Physical Modeling of Full-Field Time-Domain Optical Coherence Tomography

Andrej Keksel[1]
Institute for Measurement and Sensor-Technology, Technische Universität Kaiserslautern, Germany

Georgis Bulun
Institute for Measurement and Sensor-Technology, Technische Universität Kaiserslautern, Germany

Matthias Eifler
Institute for Measurement and Sensor-Technology, Technische Universität Kaiserslautern, Germany

Anis Idrizovic
The Institute of Optics, University of Rochester, NY, USA

Jörg Seewig
Institute for Measurement and Sensor-Technology, Technische Universität Kaiserslautern, Germany

Abstract

In this paper, a physical model of full-field time-domain optical coherence tomography (FF-TD OCT), which focuses the requirements of measuring inner textures of flexible layered samples in industrial applications, is developed and validated by reference measurements. Both the operating principle and the overall design of a FF-TD OCT correspond to that of classical white light interferometry (WLI), commonly used for the measurement of areal micro-topographies. The presented model accounts for optical and geometrical properties of the system, multiple scattering of light in turbid media and interference of partially coherent light. Applying this model, virtual measurements are used to exemplarily investigate the extent to which the principles of classical WLI can be directly transferred to obtain layer thickness measurements by simulating the use of a simple low-cost WLI system as OCT. Results indicate that a currently existing instrument setup can **only** be used as OCT to a **very limited** extent but not in general due to its initial design as a WLI.

2012 ACM Subject Classification Computing methodologies → Modeling methodologies

Keywords and phrases Optical coherence tomography, full-field time-domain OCT, virtual measuring, optical measurement technology, physical modeling

Digital Object Identifier 10.4230/OASIcs.iPMVM.2020.14

Funding This research is funded by the Deutsche Forschungsgemeinschaft (DFG, German Research Foundation) – 252408385 – IRTG 2057.

1 Introduction

In face of digitalization, industrial processes are increasingly virtualized on multiple levels. This includes the field of optical metrology, with the aim of predicting measurement results and expected uncertainties. For this purpose, the description of optical measuring instruments is increasingly based on mathematical models that represent complex physical relationships in a simplified form [29]. Such description includes a virtual measuring instrument, a virtual measuring object and, above all, the interaction between these two components [29]. The model-based prediction of measurement results can be used to, for example, analyze and optimize existing instrument setups and thus better understand the underlying processes,

[1] Corresponding author

2nd International Conference of the DFG International Research Training Group 2057 – Physical Modeling for Virtual Manufacturing (iPMVM 2020).
Editors: Christoph Garth, Jan C. Aurich, Barbara Linke, Ralf Müller, Bahram Ravani, Gunther Weber, and Benjamin Kirsch; Article No. 14; pp. 14:1–14:22
OpenAccess Series in Informatics
OASICS Schloss Dagstuhl – Leibniz-Zentrum für Informatik, Dagstuhl Publishing, Germany

or even provide insights for the development of new types of measurement systems [23]. In addition, virtual measurement data can be used for the optimization of the cost-benefit ratio in the early stages of planning a larger measurement series by estimating instrument-specific measurement uncertainties to be expected [30].

Current literature discusses a variety of physical modeling approaches, describing different optical measuring devices; these include models for describing white light interferometers [5, 28, 37], scattering light sensors [32, 37, 38, 39], atomic force microscopes [45] or X-ray computed tomography devices [10, 36].

Alternatively to the physical modeling approach, a characterization of the instrument transmission behavior, especially of topography measuring instruments, based on measurements of known geometries (represented by material measures) is a common procedure in practice. The results of this kind of empirical reference measurements can also be used for instrument specific uncertainty analyses [11] or simplified virtual measurements [17, 18].

In the context of this paper, a physical modeling approach is applied to develop a comprehensive model of an optical measuring principle – optical coherence tomography (OCT) – which is used for the characterization of intra-tissue textures. By customizing this model, for example to represent a low-cost instrument setup, it can be virtually examined to which extent this setup can be used to obtain expressive OCT measurement results.

2 Optical Coherence Tomography

Optical coherence tomography (OCT) is an optical imaging technique that allows the internal structure of scattering tissues to be imaged to micrometer resolution. OCT is mainly used in the medical sector as it enables "optical biopsy", allowing visualization of internal tissue structures without prior sample preparation. The procedure is considered to be the optical equivalent of ultrasound imaging (sonography). By using light instead of sound, OCT is limited to a lower penetration depth, but it features higher axial and lateral resolution. The most important application of OCT is currently located in ophthalmology (eye medicine). On the other hand, general suitability of OCT for industrial applications is not as explored. Selected industrial applications of OCT published are:

- Imaging fiber tows and voids in two materials: an epoxy E-glass-reinforced composite and a vinyl-ester E-glass-reinforced composite [8].
- Measurement and evaluation of the quality of the coating layer of premium glossy photopaper [22].
- Fast industrial inspection of an optical thin film panel (similar to a LCD panel) [33].
- Three-dimensional imaging of complete polymer solar cells using a high-resolution OCT system [35].
- Investigation of confocal enhanced OCT with improved image contrast and depth resolution by imaging a highly scattering paint layer [44].

Although the non-contact, non-invasive nature of the technology and its ability to image transparent, turbid and highly scattering media make the OCT technology attractive for non-destructive testing and evaluation of manufactured parts, existing instruments and their respective models are mainly designed to operate in the context of medical and biological research.

2.1 Physical measuring principle of OCT

The measuring principle of OCT is based on reconstructing cross-sectional images of intra-tissue textures using light reflections from the interior of the tissue. While the location of sound-reflecting objects is reconstructed by measuring the echo delay time in sonography, OCT uses a classical approach from optical metrology, namely coherence scanning interferometry (CSI), better known as white light interferometry (WLI) [6, 24, 43].

In a classical Michelson interferometer, the light emitted by a light source is split into two beams by a beam splitter, which are subsequently directed to the sample on the one hand and to a reference mirror on the other hand. The light beams reflected from the sample and the reference mirror are merged again afterwards, interfering with each other based on the wave properties of light. The obtained interference pattern has a high sensitivity to the path length difference between the object beam and the reference beam. Analysis of the pattern allows conclusions about positions of reflective tissue layers to be drawn. Combining classical microscopy with interferometric objectives, the micro-topography of a measuring object can be measured using the principle of CSI/WLI. By assigning a height value to every measured point, a topography map of the sample can be reconstructed. When measuring micro-topographies, monochromatic light is not typically used, but as the name "white light interferometry" already suggests, white or low-coherent light is used. The advantage of this is that the coherence length l_c of low-coherent light, which can be calculated by the properties of its spectrum, is limited to a few micrometers, so the interference pattern, which is the carrier of the height information, only occurs in a narrow height range of about $\Delta z \approx l_c$ (see also in figure 2(b)) leading to increased evaluation precision [4, 19, 24].

The principles of low-coherent interferometry described above are applied in OCT for the measurement of intra-tissue textures. There are various OCT systems whose operating principles differ greatly from each other and therefore feature different advantages and disadvantages depending on the measurement task with regard to resolution, detection speed, noise behavior, etc. In this context, a distinction is made between time-domain OCT (TD-OCT) and spectral-domain OCT (SD-OCT). Furthermore, OCT systems can be classified according to the type of lateral scanning. A distinction is made between common point-by-point scanning (flying spot) and areal measurement (wide-field or full-field OCT) [21].

The OCT model presented in this paper is based on the combination of time-domain and full-field OCT, which corresponds to the principle of a classical white-light interferometer for surface topography measurements. After validating the presented model by controlled reference measurements, it is exemplarily applied for investigating if, or under which circumstances, a custom low-cost WLI instrument setup, which is imaged in figure 7 and described in more detail in [2, 37], is suitable for the use as OCT or even as a WLI&OCT convertible instrument in general.

3 OCT model

Current literature proposes a variety of modeling approaches for OCT. These vary from very simple (single backscattering model), over very complex but restricted (extended Huygens-Fresnel based model), to very flexible but numerically complex approaches (Monte-Carlo methods combined with physically and/or statistically based models). Corresponding references are listed and summarized below.

Single backscattering model.

- In [13] a low coherence interferometry model was used to compare broadband single-Gaussian and multi-Gaussian light sources.
- In [14] an analytical model is used to simulate different optical delays in time domain OCT.
- In [25] OCT simulations has been performed using Lab VIEW and Matlab scripts.

Extended Huygens-Fresnel based model.

- In [34] an extended Huygens-Fresnel model is presented and used to describe the performance of OCT systems in both the single and multiple scattering regimes simultaneously.

Monte-Carlo model.

- In [15] a new model of OCT, which takes multiple scattering into account, is presented, combining Monte-Carlo methods and physically/statistically based models.
- In [20] a Monte-Carlo based simulator of OCT imaging for turbid media with arbitrary spatial distributions has been developed and demonstrated.
- In [40] a Monte-Carlo method for modeling OCT measurements of a diffusely reflecting discontinuity embedded in a scattering medium is presented.
- In [42] a Monte-Carlo model of steady-state light transport in multi-layered tissues has been developed and implemented.

Since the OCT model presented here is primarily intended to model industrial measurement tasks, which can be very diverse (measuring objects with different scattering properties, flexible layer structure, several light sources, lenses and objectives to choose from, etc.), a flexible and numerically efficient model is required. For this reason, the OCT model developed by the author takes into account not only the light propagation in scattering media and (partially) coherent interference properties of light, but also specific geometrical, optical and technical properties of the underlying optical system. In the next section, each of the three main components of the OCT model (optical system in section 3.1, light propagation in turbid media in section 3.2, interference behavior in section 3.3) is considered and described separately. Subsequently, the different model components are coupled and an efficient implementation (briefly described in section 3.4) is performed in order to obtain a comprehensive and at the same time fast-computing OCT model (time frame of minutes for obtaining expressive results) on which basis virtual measurements can be performed.

3.1 Optical system

The model of the optical system includes the beam paths data within the measuring instrument on the one hand and modeling of technical properties of relevant hardware components, which include lenses installed in the system, the light source, the interferometric Michelson objective and the detector on the other hand. The fundamental setup of the interferometer to be modeled is shown in figure 1.

Lenses and beam paths. When calculating the light ray paths within the optical system, the main focus lies on the lenses installed in the measuring instrument (collimator, tube and objective lenses), which are considered to have idealized properties, also known as “thin lenses” [26]. The ray paths within the measuring instrument (from the light source to the measuring object and from the measuring object to the detector) resulting from this assumption were previously derived in [37] and will be adapted in the context of the virtual FF-TD OCT to be modeled.

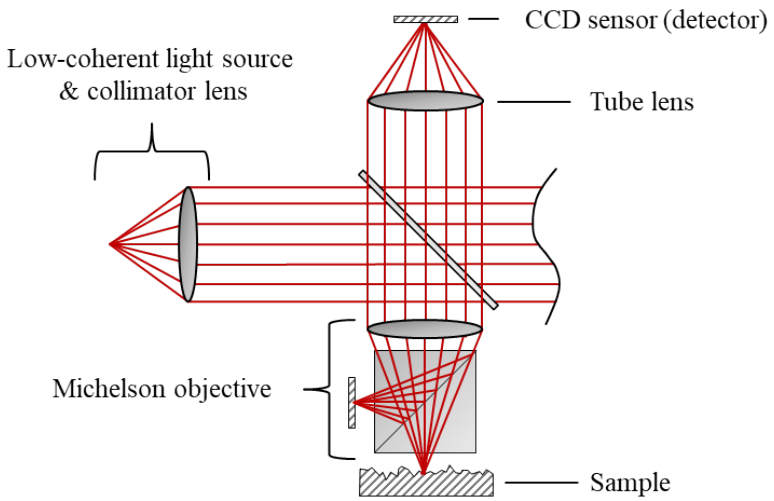

Figure 1 Schematic layout of the interferometer to be modeled.

Light source. Furthermore, the spectral properties of the light source are crucial for the function of an OCT. The electromagnetic spectrum of the light source used, which is represented by a Gaussian spectrum in figure 2 on the left, primarily describes the optical resolution limits of the measuring instrument [7]. While the lateral resolution mainly depends on the average wavelength λ_0 and the objective used (assuming the light entering the objective to be spatially incoherent [15, 16]), the axial resolution is characterized by the temporal coherence function or autocorrelation function $\gamma(\tau)$, which can be calculated according to the Wiener-Khinchin theorem by Fourier transform of the entirety of the spectrum of light used ($S(\lambda)$ in terms of wavelength λ, or $S(\nu)$ in terms of frequency ν) [6]:

$$\gamma(\tau) \sim \int_0^\infty S(\nu) \cdot \exp(-i2\pi\nu\tau) d\nu \tag{1}$$

Note that the integral only has to cover positive values since a light spectrum is exclusively composed of positive wavelengths/frequencies. In general, the axial resolving capability increases with increasing bandwidth. The real part of the autocorrelation function is shown in figure 2b and corresponds to an ideal correlogram resulting from the interference of sample and reference beam, on the basis of which measurement signals are evaluated in CSI/WLI and TD-OCT.

Another important property of light in OCT is the maximum penetration depth into the measuring sample. This also depends on the light spectrum used. In OCT measurements of biological tissue, light in the near-infrared range (wavelengths in the range of $\lambda = 650 \ldots 1350\,nm$) is commonly used, since the absorption of light in biological tissue is minimized in that wavelength range [7].

In summary, for high-resolution OCT applications, a light source with the broadest possible spectrum (high axial resolution) in the near-infrared range (high penetration depth) is recommended.

Interferometric Michelson objective. Other important components of the optical system are the interferometric objectives, which fundamentally differ in their design. The three basic designs are the Michelson, Mirau and Linnik designs [27]. In a Michelson objective

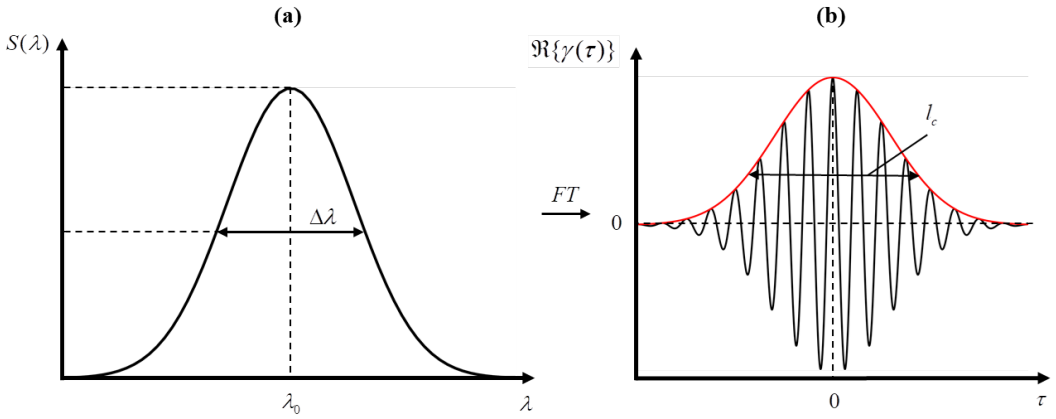

Figure 2 (a) Exemplary Gaussian light spectrum $S(\lambda)$ and (b) the real part of the corresponding autocorrelation function $\Re\{\gamma(\tau)\}$ with plotted envelope (red) and coherence length $l_c \approx \lambda_0^2/\Delta\lambda$.

(figure 3), a beam splitter is mounted below the focusing lens. This separates the incident light beam into sample and reference beam. The reference mirror is mounted on the side of the beam splitter. This design is only used for objectives with a low magnification ($\leq 10\times$), which have a larger focal length due to the limited space available and thus low numerical aperture (NA) [27]. An appropriate model of a Michelson objective is provided by following parameters: Numerical aperture (NA), beam splitting ratio of the beam splitter (ρ) and reflectance of the reference mirror (r_R). While NA represents a geometric parameter, ρ and r_R represent light intensity ratios. The beam splitting ratio ρ describes the intensity ratio between the reference beam and the sample beam, and the reflectance of the reference mirror r_R represents the ratio of the intensities of the reference beam after and before the reflection takes place.

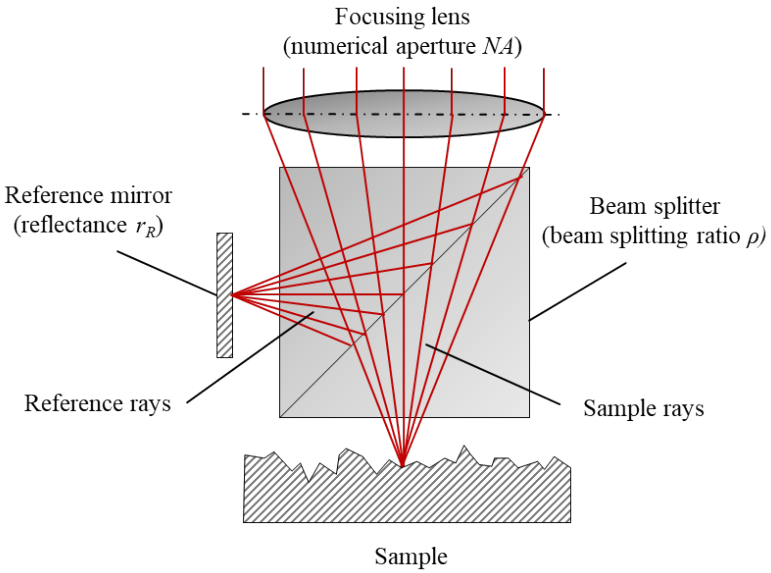

Figure 3 Michelson objective.

The modeling of the detector within this work is mainly limited to pixel size and with this the optical system to be modeled is fully characterized.

In the next section, the Monte-Carlo based modeling approach used to describe light propagation in turbid media is summarized.

3.2 Light propagation in turbid media

The light-matter interaction in the context of OCT depends both on the properties of the incident light and on the optical properties of the illuminated sample. The interplay of these properties defines the reflection, transmission, absorption and scattering behavior as well as changes in the polarization states. There are various material-specific optical parameters that describe the interaction of light and matter. These include:

- Refractive index n (reflection and transmission behavior)
- Absorption coefficient μ_a (absorption behavior)
- Scattering coefficient μ_s (scattering behavior)
- Anisotropy factor g (degree of directional change due to scattering)

It should be noted that each of these optical material properties is generally wavelength-dependent [43]. A frequently used approach for the description of light transport in multi-layered tissue using the material-specific optical parameters mentioned above is the Monte-Carlo based MCML algorithm of Wang et al. [12, 42], which is adapted here in a customized version. This approach considers light in the form of photons, or photon packages. The propagation of light is characterized by a large number of photons which are emitted by the light source and whose trajectory and intensity changes induced by reflection, transmission, scattering and absorption processes are calculated by statistical methods. The implemented customizations of the MCML algorithm are the following:

- The assumption of orthogonal and point-wise light irradiation of the tissue is replaced by the model of a focused light beam (focusing properties according to the NA of the Michelson objective used).
- The Henyey-Greenstein scattering function for the description of the material's scattering properties is replaced by the **extended** Henyey-Greenstein scattering function, also known as Cornette-Shanks phase function [3, 41], which provides a more realistic scattering pattern.
- The light rays do not experience ideal reflection or transmission when hitting an interface but are subject to roughness induced scattering, also described by the extended Henyey-Greenstein scattering function.

In figure 4, exemplary trajectories of the modeled light-matter interaction of a light beam hitting the surface of two composites perpendicularly are shown on the right. The samples are surrounded by air and are modeled as two-layered composites of glass (figure 4a) and turbid tissue (figure 4b). The corresponding optical material parameters, as well as the geometrical sample properties are summarized on the left-hand side of figure 4.

Combining the trajectories of the scattered photons within the tissue and the modeled ray paths within the optical system, the entire trajectory of a photon emitted by the light source, hitting the sample and being reflected towards the detector is fully described. At the plane of the intensity-sensitive detector, the interference of the reference and sample beam is made visible. The mathematical description of the partially coherent interference behavior at the detector plane represents the third pillar of the OCT model, which is explained in the following section.

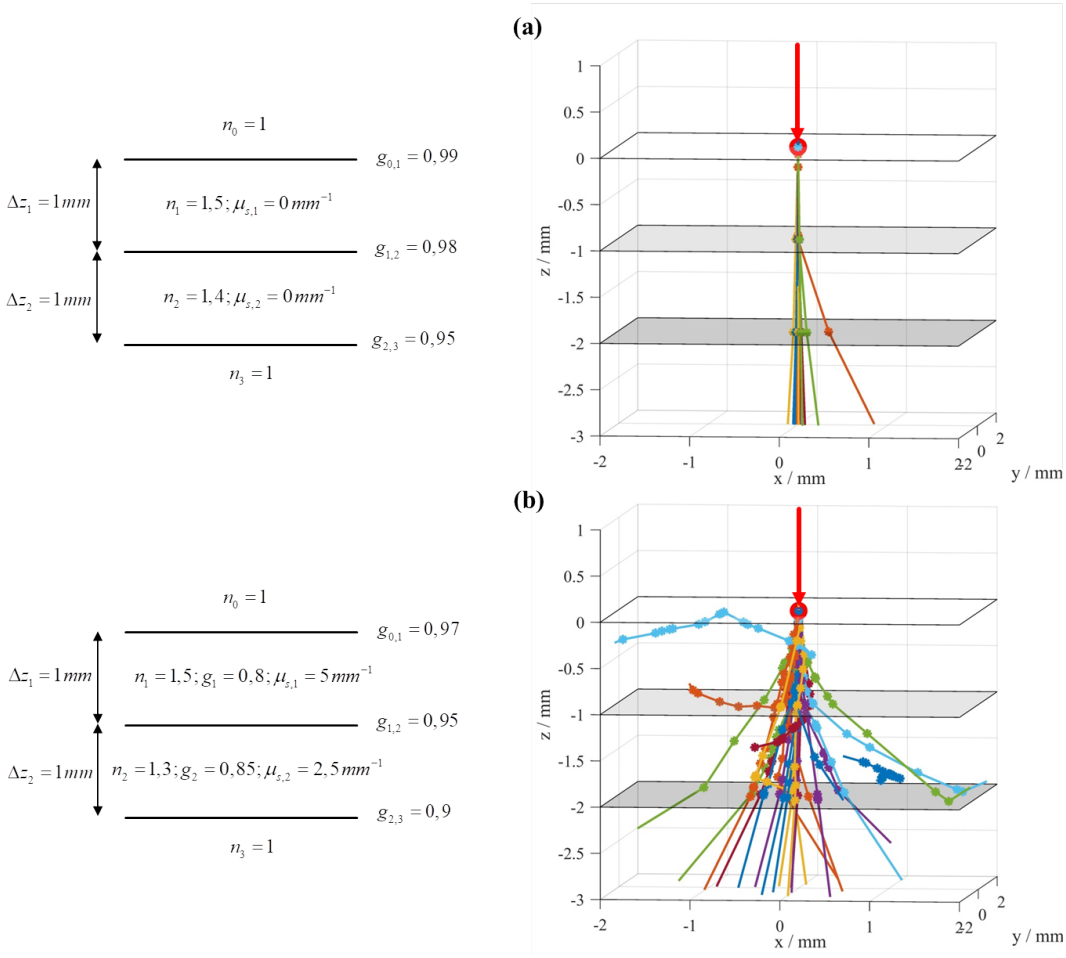

Figure 4 Geometrical properties and optical parameters of the modeled material composites (left) and 25 exemplary simulated photon trajectories resulting from the light-matter interaction of orthogonal illumination (right) of a two-layered glass composite (a) and a two-layered biological tissue (b).

3.3 Interference properties

The interference properties of the sample beam and the reference beam are modeled by classical Fourier optics [9], considering a scattered and therefore attenuated sample beam. For this purpose, both temporal and spatial coherence properties of light must be taken into account. The temporal coherence properties of a light source, key for the axial resolving capability of the measuring instrument, are entirely defined by its spectrum. This is not the case for the spatial coherence properties, which mainly influence the lateral resolution of the measuring instrument. In the context of this paper, a spatial coherence model is applied, where only two absolute modes – completely spatially coherent and completely spatially incoherent superposition of reference and sample beams – are distinguished. According to [15, 16] this assumption is valid if the light entering the objective is provided by uniformly bright spatial incoherent light, which is also a requirement for a FF-TD OCT system and thus installed in the current instrument setup. Whether reference and sample beams are coherently superimposed at the detector plane depends on their light source origin (which

must be the same for reference and sample photons), their optical path differences (which must be within the coherence length of the light to be considered as temporal coherent to each other) and their detector hitting points relative to each other (which must be within the range of the Airy disk to be considered as spatial coherent to each other). This model of coherence domain limitation corresponds to the "coherence volume" model from [15, 16]. According to this model, the Airy disk provides the lateral limitation of the coherence volume, which is, according to the Rayleigh criterion, also a measure of the achievable lateral resolution of the measuring instrument [1]. The coherence length of the light is a measure of axial limitation of the coherent volume. Based on this model, signal formation on the detector as a result of coherent as well as incoherent superposition of reference and scattered sample beams or photons is described below.

In the simplest case of ideal low-coherent two-beam interferometry, the detector signal I_D can be classically determined according to following equation [5]

$$I_D(\tau) = I_R + I_S + 2 \cdot \sqrt{I_R \cdot I_S} \cdot \Re\{\gamma(\tau)\}, \tag{2}$$

whereby I_R and I_S represent the intensities of mutually-coherent reference and sample beams, τ represents the optical path difference between the reference beam and the sample beam, and γ represents the normalized temporal coherence function (or autocorrelation function) of the light used. However, in the OCT model presented here, both the reference and sample beams are described as the sum of a large number of individual and potentially scattered photons that originate from different points of the areal light source, hit the detector on various positions with different intensities and optical path differences relative to each other and are not necessarily mutually-coherent. Therefore, the description of the detector signal must be modified accordingly. The photon-wise composition of the detector signal is visualized in figure 5. The calculation is assuming a gridded detector plane, in which each grid cell represents a coherence region of the reference beam hitting the detector. To describe the composition of the detector signal in figure 5b, the blue marked coherence region in the center of figure 5a serves as a representative coherence region of the detector.

The reference beam, or the sum of the photons forming it, is not scattered in the model. As a result, a beam ideally focused on the detector (red or black dot) assumed to be spatially incoherent creates a coherence region around itself equal to the size of the (magnification-scaled sample-plane) Airy disk, which is approximated here as an equally sized square (blue square). The intensity of the reference beam depends on the number of reference photons hitting the detector and their individual intensities. When describing the sample beam, which is also composed of a multitude of scattered photons, a distinction must be made between sample photons that are coherent and those that are incoherent to the reference beam, since coherent superposition and incoherent superposition of reference and sample beams are fundamentally different. Mathematically, the interaction of the electric/magnetic fields can be easily described by summing up the individual photon intensities in the case of incoherent superposition, which is not the case when considering the superposition to be coherent. Both the sample beam photons that are coherent to the reference beam (red crosses, originate from the same point as the reference beam represented by the red dot) and those that are incoherent to it (gray crosses, originate from other points than the reference beam represented by the red dot) hit the detector within the observed coherence region. Since sample photons experience individual scattering and absorption when interacting with the sample to be measured, their intensities and optical path differences relative to the corresponding reference path must be tracked individually and the number of photons hitting the representative region of the detector (mutually coherent and mutually incoherent) has to be counted. It

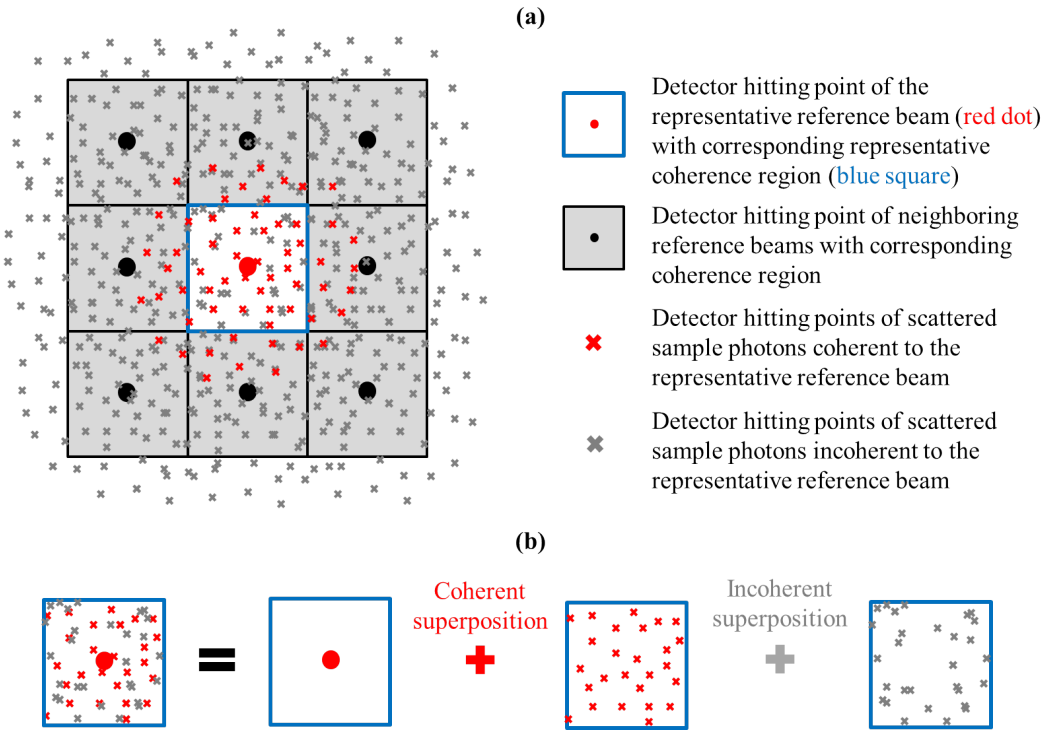

Figure 5 (a) Grid of the detector plane with visualization of the detector hitting points of exemplary reference and sample photons; (b) Composition of the detector signal consisting of reference beam, sample photons coherent and sample photons incoherent to it.

should be mentioned that only the mutually coherent sample photons (red crosses) contribute to the information-containing signal formation. The scattering-induced "cross-talk" between mutually incoherent reference and sample photon pairs (gray crosses hitting the representative blue marked region) does not provide any valuable height information, but only leads to a reduction of the signal-noise ratio by increasing the total intensity.

Based on this model of signal formation, the three summands in (2) have to be replaced by modified terms. It should be noted that only the photons hitting the representative coherence region (blue marked square) are considered forming the signal.

The intensity of the reference beam $I_{R,\Sigma}$ (red dot) depends on the number of reference photons hitting the detector $k_{R,Det}$ and their individual intensities, whereby the individual intensity of a reference photon is obtained by

$$i_R = \rho^2 \cdot r_R \cdot i_0, \tag{3}$$

considering the initial photon intensity i_0, the photon passing the beam splitter twice ($i_R \sim \rho^2$) and taking into account the reflectivity of the reference mirror ($i_R \sim r_R$). Accordingly, $I_{R,\Sigma}$ is determined by

$$I_{R,\Sigma} = k_{R,Det} \cdot i_R. \tag{4}$$

This term (4) substitutes the first summand of (2).

The situation is similar for the photons of the sample beam hitting the detector $I_{S,\Sigma}$. Sample beam photons that are both coherent (red crosses) and incoherent (gray crosses) to the reference beam hit the detector within the representative coherence region (blue square).

Since sample photons experience individual scattering and absorption when interacting with the sample to be measured, their intensity must be determined individually and the number of photons hitting the representative section of the detector must be counted. The individual intensity of a sample photon $i_{S,j}$ is obtained by

$$i_{S,j} = (1-\rho) \cdot [i_0 \cdot (1-\rho) - i_{a,j}], \tag{5}$$

considering the photon passing the beam splitter twice and experiencing an individual absorption-related intensity loss $i_{a,j}$. Accordingly, $I_{S,\Sigma}$ is determined by

$$I_{S,\Sigma}(z) = \sum_{j=1}^{k_{S,Det}(z)} i_{S,j}, \tag{6}$$

where $k_{S,Det}(z)$ is the number of sample photons hitting the representative coherence region at scan position z, regardless of whether they are coherent to the reference beam. The term in (6) substitutes the second summand of (2).

The substitution of the third summand from (2) results from the coherent superposition of reference and sample photons. In addition to the number and intensity of the mutually-coherent reference and sample photons hitting the detector at scan position z, their optical path difference to each other τ combined with the temporal coherence function $\gamma(\tau)$ of the light used affect the signal formation. This relationship is described by

$$I_{c,\Sigma}(z) = 2 \cdot \sqrt{I_{R,\Sigma} \cdot |IA_{S,c,\gamma,\Sigma}(z)|} \cdot \operatorname{sgn}(IA_{S,c,\gamma,\Sigma}(z)) \tag{7}$$

whereby

$$IA_{S,c,\gamma,\Sigma}(z) = \sum_{j=1}^{k_{S,c,Det}(z)} i_{S,c,j} \cdot \Re\{\gamma(\tau_j)\} \cdot |\Re\{\gamma(\tau_j)\}|. \tag{8}$$

The term $k_{S,c,Det}(z)$ corresponds to the number of sample photons that hit the relevant detector section at scan position z and are coherent to the reference beam, $i_{S,c,j}$ represents their individual intensity and τ_j their individual optical path difference to the reference beam. The expression for $IA_{S,c,\gamma,\Sigma}(z)$ thus corresponds to the intensity-weighted sum of coherent sample photons combined with their respective contribution to the alternating interference signal component. The terms in (7) and (8) are expressed in this cumbersome way to avoid negative square root entries. A comparison of the idealized detector signal described in (2) and the photon-wise composition described in (4)-(8) is visualized in figure 6.

3.4 Coupling and Implementation

At this point, by adding white noise to the simulated signal, the signal formation of a virtual OCT measurement starting with the photon emission in the light source and finishing with the signal acquisition on the detector plane is fully described. Based on this description the simulations can be carried out by emitting a large number of photons and monitoring their trajectories and intensities until they hit the detector plane. With a time domain OCT (TD-OCT) method to be modeled in this paper, these calculations would have to be performed for each discrete cross-sectional height cut of the vertical scanning process. To reduce the computing effort of the virtual OCT measurement, the number of photon trajectories to be calculated must be reduced without reducing the validity of the simulation

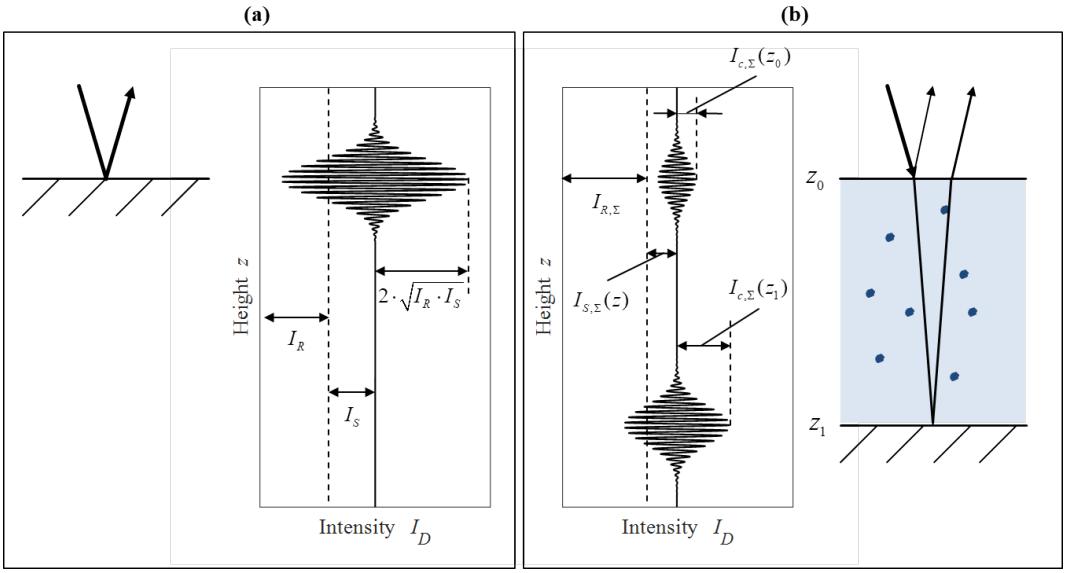

Figure 6 Illustration of the detector signal composition for (a) the idealized WLI measurement model in (2) (assuming specular reflection of light illuminating a mirror-like surface) and (b) the photon-wise composition model in OCT described in (4)-(8) (assuming partial reflection of light illuminating a layered tissue sample containing scatterers/absorbers).

result. This is done by exploiting the geometric conditions and by multiple adaptions of representative photon trajectories, which have been calculated once, thus drastically reducing the computing effort for the scanning process to be simulated by an upscaling method.

In the next section, the model is validated using real measurements performed by a reference instrument setup (which was initially designed as WLI) used as OCT. In the first step, the measurement conditions are provided to be idealized and thus should not be challenging from a measurement technology point of view. This is ensured by varying layer structures composed of only weakly light-scattering media (glass plates, air, specular reflecting surface). Based on this, the limitations of the current instrument setup will be explored by virtually increasing the difficulty of the measurement conditions. This will be done by virtually measuring thicker, optical rougher and more turbid (and therefore more challenging) virtual samples.

4 Validation of the OCT model

The first step towards validation of the OCT model is to create a virtual replica of the reference instrument. The reference instrument and the spectral properties of the (visual red) light source used for this purpose are visualized in figure 7. On the basis of this instrumental setup, an initial comparison of real and virtual measurements is carried out using three exemplary measuring tasks that are not very challenging in terms of measurement technology and comparatively easy to parameterize. The three measuring tasks under investigation are based on a simple bridge-like structure of identical glass plates on a specular surface as shown in figure 8. Thus, three differently structured measurement tasks can be taken from a single areal OCT measurement. These correspond to the following structures:

(a) specular reflecting surface (no layers to penetrate)
(b) glass layer – specular reflecting surface (one layer to penetrate)
(c) glass layer – air layer – specular reflecting surface (two layers to penetrate)

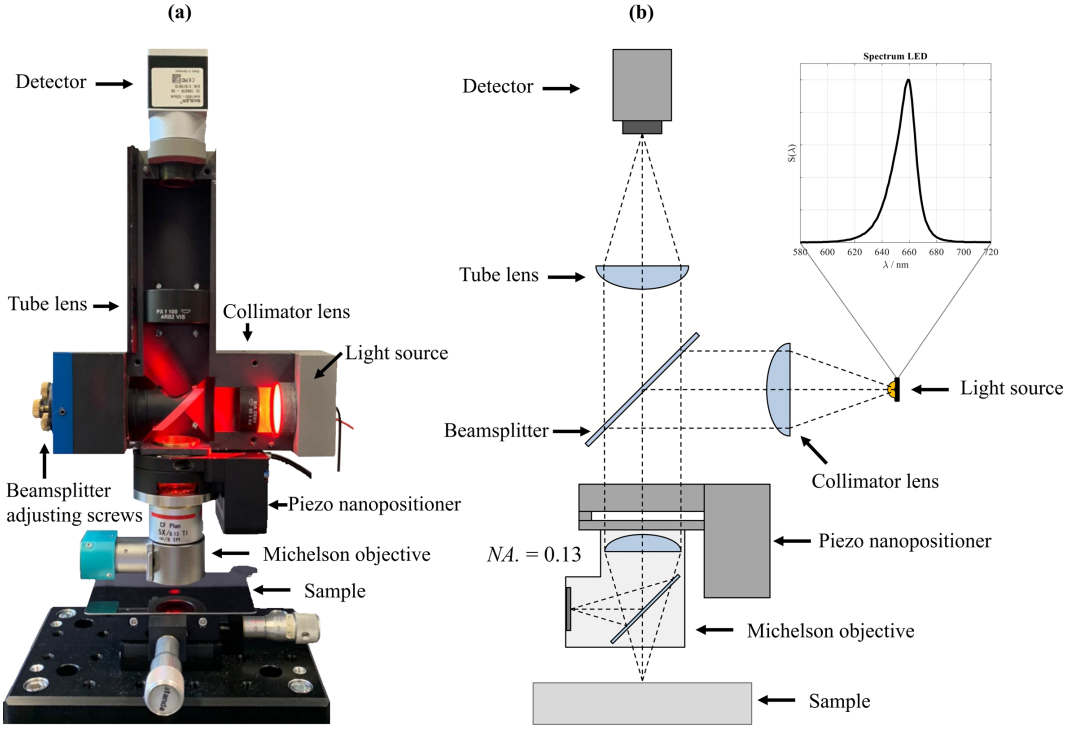

Figure 7 (a) Reference and (b) virtual instrument setup used for the validation of the OCT model.

Theoretically, a fourth measuring task (glass layer – glass layer – specular reflecting surface) could be extracted from the measurement setup visualized in figure 8, which is waived at this point since the optical height of this stack exceeds the scanning range of the piezo nanopositioner installed in the instrument.

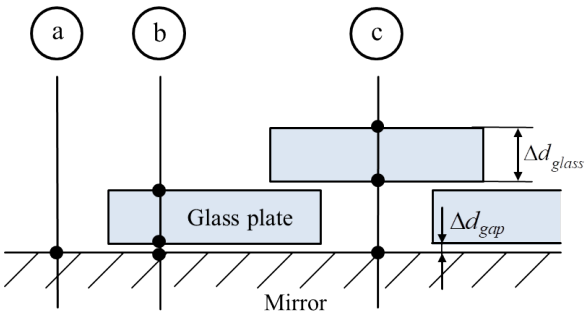

Figure 8 Measurement setup used to match virtual and real measurements. Labels 1 to 3 mark the three positions where the characteristic measurement signals were extracted from. The small black dots mark positions where the light interacts with boundary layers.

The simplicity of the parameterization of the optical material properties is based on the transparency of glass and air layers (no scattering or absorption, $\mu_s = \mu_a = 0$) as well as the (almost) ideal reflection properties of a flat mirror surface (ideally specular reflection, $g_{mirror} = 1$) provides the initial comparison of virtual and real measurements. The variable

Table 1 Estimated device and material properties of the measurement system provided by performed matching of virtual and reference measurement signals.

Device properties	
ρ	0.6
Material properties	
Δd_{glass}	106 µm
Δd_{gap}	31 µm
n_{glass}	1.53
$g_{surface}$ (optical surface roughness)	0.985

optical material properties are reduced to the refractive index (n_{glass}) and the optical surface roughness of the glass layer (here expressed by the anisotropy factor $g_{surface}$). Thus, the unknown (optical) instrument and material properties can be provided by performing a simple trial&error matching of simulated virtual measurement and the real measurement signals, which is done by comparison of respective signal amplitudes obtained. The matched signals are visualized in figure 9 and the unknown optical parameters determined on the basis of this procedure are summarized in table 1.

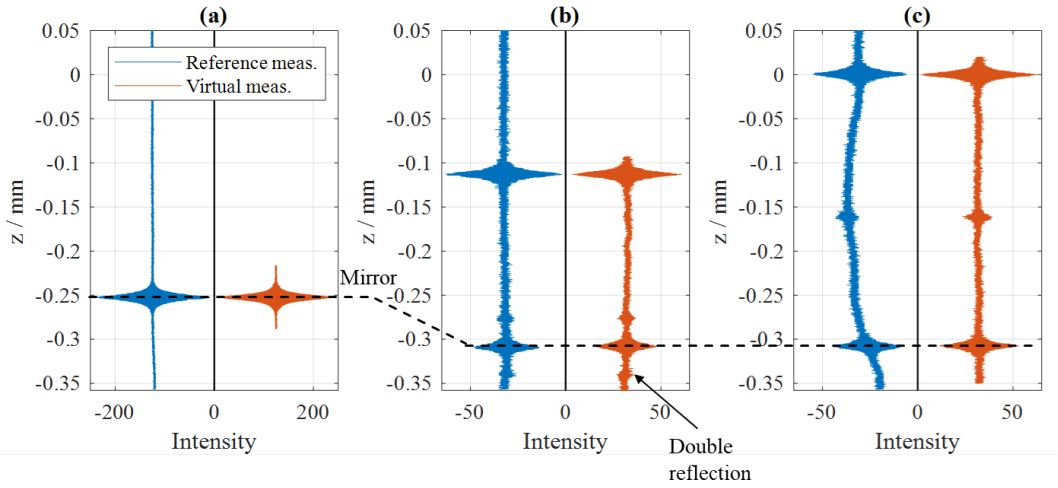

Figure 9 Comparison of measured (blue – left-hand side) and modeled (red – right-hand side) signals for the cases of measuring (a) the mirror surface, (b) the glass layer – mirror surface structure and (c) the bridge-like glass layer – air layer – mirror surface structure visualized in figure 8.

By setting the unknown modeling parameters in accordance to the values given in table 1, a high level of congruence between modeled and measured signals is achieved, which is imaged in figure 9. In the following, the physical limitations of the current instrument setup used as OCT are exemplarily explored using virtual measurements. For this purpose, a single-layered structure (tissue layer on a specular reflecting surface) is modeled as getting thicker ($\Delta z \uparrow$), optical rougher ($g_{surface} \downarrow$) and more turbid ($\mu_s \uparrow, \mu_a \uparrow, g \downarrow$) and thus the corresponding virtual measurement results are generated and evaluated.

Table 2 Instrument and material parameters chosen for the **full factorial** study of virtual measurements of the three cases (a)-(c) mentioned.

Instrument/ material parameter	(a) Variation of thickness	(b) Variation of optical roughness	(c) Variation of turbidity
NA	$[0.07 \quad 0.1 \quad 0.13]$	0.13	0.13
$\Delta z/mm$	$[0.05 \quad 0.1 \quad \ldots \quad 0.8]$	$[0.1 \quad 0.2 \quad 0.3]$	$[0.1 \quad 0.2 \quad 0.3]$
$g_{surface}$	0.985	$[1 \quad 0.99 \quad \ldots \quad 0.8]$	0.985
μ_s/mm^{-1}	0	0	5
μ_a/mm^{-1}	0	0	0.5
g	–	–	$[1 \quad 0.99 \quad \ldots \quad 0.8]$

5 Virtual measurements

The modeled setup for the virtual measurements, consisting of a single tissue layer placed on a specular reflecting mirror, is shown in figure 10. In the first measurement task to be

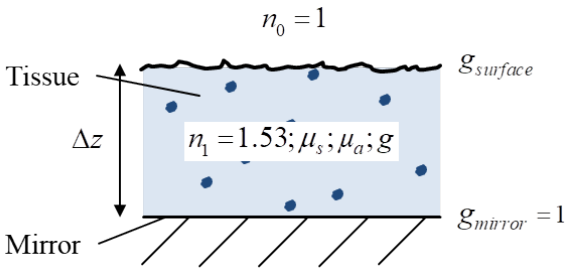

Figure 10 Measurement model of a single-layered tissue placed on a specular reflecting mirror.

modeled, the effect of a variation in the thickness Δz of the previously used glass plate on the measurement result is investigated given three Michaelson objectives with varying NA. Hereby it can be estimated where the limitations of the used instrument setup lie at almost ideal measurement conditions. Furthermore, it is investigated how a variation of the (optical) surface roughness, represented by the coefficient $g_{surface}$, affects the measurement result assuming other conditions to be constant and almost ideal. This describes, for example, the film thickness measurement of clear coatings which cause a certain surface roughness. This case is also investigated for variable film thicknesses. Finally, by varying scattering, absorption and anisotropy coefficients μ_s, μ_a and g, turbid tissue is modeled and the influence of these material parameters on the measurement result, assuming the layer thickness and surface roughness remaining constant, is investigated. This case corresponds, for example, to the layer thickness measurement of biofilms cultivated on smooth and thus specular reflecting surfaces. The instrument and material parameters chosen for the full factorial study of each of these cases are listed in table 2 and corresponding results of the virtual measurements are shown and evaluated in figure 11.

The investigation of the suitability of the current instrument setup for the various measuring tasks described above is based on the detectability of the signal component that can be assigned to the light reflection of the mirror. For this purpose, virtual measurements are performed and the generated intensity signals are evaluated by their envelope, which can be generated using Hilbert transform [31]. Since the geometrical and optical properties of

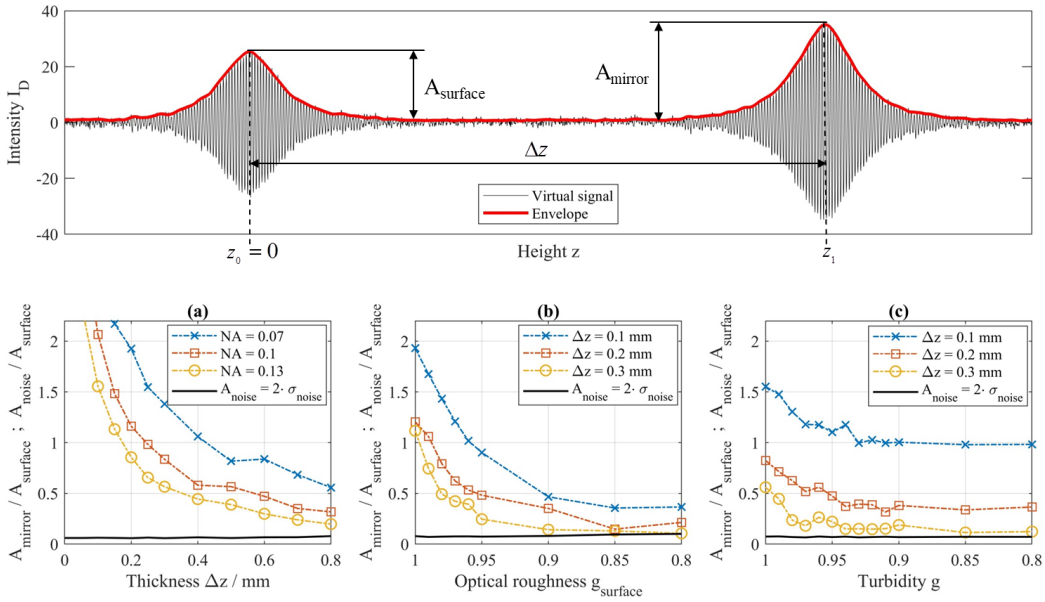

Figure 11 Results extracted from virtual measurements considering three different measuring tasks. Top: Exemplarily virtual measuring result and its envelope. Bottom: Evaluation of the virtually measured intensity signals using the parameters summarized in table 2 by plotting the amplitude ratio of mirror and surface reflection signal components against the disturbance variables (a) thickness, (b) optical surface roughness and (c) turbidity (represented by the anisotropy coefficient g). As a comparable measure of the instruments noise the ratio of $2 \cdot \sigma_{noise}$ and the amplitude of the surface reflection component is plotted as well.

the virtually measured sample match the dimensions of the experimental sample for which the OCT model was validated it is legitimate to evaluate the capabilities of the instrument to characterize samples of increasing level of complexity exclusively by performing virtual measurements. The upper part of figure 11 shows an example of a generated measurement signal including the generated envelope. By calculating the signal amplitude ratio between the intensity components of the surface and the mirror reflection while increasing the individual disturbance variables (layer thickness Δz, optical surface roughness $g_{surface}$, turbidity $\begin{bmatrix}\mu_s & \mu_a & g\end{bmatrix}$) and comparing it with the instrument's noise, which is also related to the surface reflection, the limits of the current instrument setup can be identified. The lower limit of the detectability is defined at this point by twice the standard deviation of the instrument's noise.

In general, it can be seen from the lower part of figure 11 that when the disturbance variables are increased, the intensity of the measured signal component reflected by the mirror decreases very sharply.

In the first case considered in (a), the dependence on the NA of the (Michelson) objective used is shown in addition to the strong dependence of the sample layer thickness. As described in [7], the dependence on the objectives NA can be explained by the displacement of the focal and coherence plane within the sample, which the reference beam does not experience and thus the ability for coherent interference is reduced. However, changing the lens actually used in this work ($NA = 0.13$) would not lead to an optimization of the instrument setup at this point, since the scanning range is limited to <400 µm. If this range is increased, however, the use of an objective with a smaller NA could be quite reasonable.

In the second case considered in (b) it can be observed that the optical surface roughness of the sample also has a strong influence on the signal quality. Due to increasing initial light scattering at the height level of the sample surface, the number of photons coherent to the reference beam hitting the coherence region (figure 5) decreases. According to the virtual measurements carried out here, even a small optical surface roughness ($g_{surface} < 0.9$) can cause the detectability of the signal component assigned to the mirror to fall below the noise level of the measuring instrument. A reduction of the noise level, e.g. by using a camera sensor system optimized for the light spectrum used, could remedy this situation.

In the third case considered in (c) it can be observed that especially the combination of turbidity and thickness of the tissue layer to be penetrated affects the quality of the measurement result. The decline in the signal amplitude ratio between surface and mirror reflection does not occur as abruptly with increasing turbidity as, for example, with surface roughness increments. More important in the context of measurability of turbid tissue is the "optical depth" (OD) [43], which is measured as

$$OD = (\mu_s + \mu_a) \cdot \Delta z. \tag{9}$$

6 Comments on a WLI&OCT convertible

Although WLI and OCT are based on the same measuring principle, the virtual measurements carried out above have shown that the current instrument setup can only be used as OCT for layer thickness measurements within highly restricted boundary conditions. This includes, for example, layer thickness measurements of thin, smooth and (partially) transparent materials, such as glass plates (see experiment), foils, transparent coatings or the detection of air inclusions, etc. The strong limitation of using the current instrument setup as OCT is due to several limiting factors. These include

- the height shift of the focal plane (lengthens within a refractive tissue) in relation to the coherence plane (shortens within a refractive tissue) of a focused light beam [7],
- the use of visual red light instead of near-infrared light,
- optical and technical components designed for the use of visual light (lenses, beam splitters, detector) and
- the maximum scanning range of <400 µm.

A very simple way to achieve an easy optimization of the current instrument setup towards application as OCT would be the use of an objective with low NA combined with an adjustable beam splitting ratio (both not available at the time of writing). By attenuating the intensity of the reference beam, the signal-noise ratio could be increased, which in turn increases the bandwidth of measurable structures. However, overall, the current instrument setup is not suitable for the use as OCT in context of diverse industrial applications, although the physical measuring principle corresponds to WLI.

7 Conclusion

Within this paper, a physical model of full-field time-domain optical coherence tomography (FF-TD OCT), which focuses the requirement of (virtually) measuring flexible layered structures, was developed, validated and exemplarily applied to investigate the extent to which the principles of classical WLI can be directly transferred to obtain layer thickness measurements by a using a simple low-cost instrument as WLI&OCT convertible. The developed model takes into account the optical and geometrical properties of the system

used (linear optics), as well as the light propagation in light scattering media (Monte-Carlo based modeling), and corresponding interference properties (partially coherent interference of light). The validation of the model was carried out on the basis of reference measurements. Three differently structured and highly controlled measurement tasks were used for this purpose. Subsequently, the knowledge gained from the validation was used to carry out virtual measurements of measuringt tasks with increased complexity (thicker layers, optically rougher surfaces, turbid tissue). On the basis of these virtual measurements, a first impression of the influence of various parameters and disturbance variables on the expected measurement result was given. It was shown that a currently existing low-cost WLI instrument setup cannot be used as OCT in general, but only to a very limited extend. The limitations are largely caused by the fact that the instrument was initially designed as WLI.

In future works, a FF-TD OCT optimized for industrial purposes will be realized with the aid of the OCT model developed in this paper.

Nomenclature and List of Abbreviations

Δd	layer thickness
Δz	height range, layer thickness
$\Delta\lambda$	full width at half maximum
γ	temporal coherence function
λ	wavelength of light
λ_0	average wavelength of light
μ_a	absorption coefficient
μ_s	scattering coefficient
ν	frequency of light
$\Re$	real part of complex number
ρ	beam splitting ratio
σ_{noise}	standard deviation of instrument noise
τ	optical path difference
A	amplitude
g	anisotropy factor
$g_{surface}$	optical surface roughness
i_0	initial intensity of an emitted photon
I_D	detector intensity
I_R	reference beam intensity
i_R	intensity of a single reference photon
I_S	sample beam intensity
i_a	absorption-related intensity loss
$I_{c,\Sigma}$	coherent intensity component
$I_{R,\Sigma}$	sum of reference photon intensities
$I_{S,\Sigma}$	sum of sample photon intensities
$i_{S,c}$	intensity of a single coherent sample photon
i_S	intensity of a single sample photon
$IA_{S,c,\gamma,\Sigma}$	intensity-weighted sum of coherent sample photons combined with their respective contribution to the alternating interference signal component
$k_{R,Det}$	number of reference photons hitting the detector
$k_{S,c,Det}$	number of coherent sample photons hitting the detector
$k_{S,Det}$	number of sample photons hitting the detector

l_c	coherence length of light
n	refractive index
NA	numerical aperture
OD	optical depth
r_R	reflectance of reference mirror
S	spectrum of light
z	height, scan position
CCD	charge coupled device
CSI	coherence scanning interferometry
FF	full field
FT	Fourier transform
LCD	liquid crystal display
MCML	monte carlo modeling of light transport
OCT	optical coherence tomography
SD	spectral domain
TD	time domain
WLI	white light interferometry

References

1. Max Born, Emil Wolf, and Avadh Behari Bhatia. *Principles of optics: Electromagnetic theory of propagation, interference and diffraction of light*. Cambridge Univ. Press, Cambridge, 7th ed., 11th reprinting edition, 2016.
2. Georgis Bulun, Matthias Eifler, Julian Hering, Georg von Freymann, and Jörg Seewig. Performance specification of areal surface texture instruments exemplified by a self-built wli. In Michael B. North Morris, Katherine Creath, and Rosario Porras-Aguilar, editors, *Interferometry XX*, page 15. SPIE, 2020. doi:10.1117/12.2567666.
3. William M. Cornette and Joseph G. Shanks. Physically reasonable analytic expression for the single-scattering phase function. *Applied optics*, 31(16):3152–3160, 1992. doi:10.1364/AO.31.003152.
4. Peter de Groot. Principles of interference microscopy for the measurement of surface topography. *Advances in Optics and Photonics*, 7(1):1, 2015. doi:10.1364/AOP.7.000001.
5. Peter de Groot and Xavier Colonna de Lega. Signal modeling for low-coherence height-scanning interference microscopy. *Applied optics*, 43(25):4821–4830, 2004. doi:10.1364/AO.43.004821.
6. Wolfgang Drexler. *Optical coherence tomography: Technology and applications /Wolfgang Drexler ... (eds.)*. Biological and Medical Physics, Biomedical Engineering. Springer, Berlin and Heidelberg, 2008.
7. Arnaud Dubois, editor. *Handbook of full-field optical coherence microscopy: Technology and applications*. Pan Stanford Publishing, Singapore, 2016.
8. Joy P. Dunkers, Richard S. Parnas, Carl G. Zimba, Richard C. Peterson, Kathleen M. Flynn, James G. Fujimoto, and Brett E. Bouma. Optical coherence tomography of glass reinforced polymer composites. *Composites Part A: Applied Science and Manufacturing*, 30(2):139–145, 1999. doi:10.1016/S1359-835X(98)00084-0.
9. Joseph W. Goodman. *Introduction to fourier optics*. W.H. Freeman Macmillan learning, New York, fourth edition edition, 2017.
10. Shengling Huang, Xin Wang, Yifan Chen, Jie Xu, Tian Tang, and Baozhong Mu. Modeling and quantitative analysis of x-ray transmission and backscatter imaging aimed at security inspection. *Optics express*, 27(2):337–349, 2019. doi:10.1364/OE.27.000337.
11. ISO 25178–70. Geometrical product specifications (gps) – surface texture: Areal —- part 70: Material measures (iso 25178–70:2014), 2014.

12 Steven L. Jacques. Modeling tissue optics using monte carlo modeling: A tutorial. In Steven L. Jacques, William P. Roach, and Robert J. Thomas, editors, *Optical Interactions with Tissue and Cells XIX*, SPIE Proceedings, page 68540T. SPIE, 2008. doi:10.1117/12.776997.

13 Paul Jansz, Steven Richardson, Graham Wild, and Steven Hinckley. Modeling of low coherence interferometry using broadband multi-gaussian light sources. *Photonic Sensors*, 2(3):247–258, 2012. doi:10.1007/s13320-012-0069-0.

14 Paul Jansz, Graham Wild, Steven Richardson, and Steven Hinckley. Simulation of optical delay lines for optical coherence tomography. In *2011 International Quantum Electronics Conference (IQEC) and Conference on Lasers and Electro-Optics (CLEO) Pacific Rim incorporating the Australasian Conference on Optics, Lasers and Spectroscopy and the Australian Conference on Optical Fibre Technology*, pages 1400–1402. IEEE, 2011. doi:10.1109/IQEC-CLEO.2011.6194128.

15 Boris Karamata, Markus Laubscher, Marcel Leutenegger, Stéphane Bourquin, Theo Lasser, and Patrick Lambelet. Multiple scattering in optical coherence tomography. i. investigation and modeling. *Journal of the Optical Society of America. A, Optics, image science, and vision*, 22(7):1369–1379, 2005. doi:10.1364/JOSAA.22.001369.

16 Boris Karamata, Marcel Leutenegger, Markus Laubscher, Stéphane Bourquin, Theo Lasser, and Patrick Lambelet. Multiple scattering in optical coherence tomography. ii. experimental and theoretical investigation of cross talk in wide-field optical coherence tomography. *Journal of the Optical Society of America. A, Optics, image science, and vision*, 22(7):1380–1388, 2005. doi:10.1364/JOSAA.22.001380.

17 Andrej Keksel, Matthias Eifler, and Jörg Seewig. Modeling of topography measuring instrument transfer functions by time series models. *Measurement Science and Technology*, 29(9):095012, 2018. doi:10.1088/1361-6501/aad467.

18 Andrej Keksel, Anna-Pia Lohfink, Matthias Eifler, Christoph Garth, and Jörg Seewig. Virtual topography measurement with transfer functions derived by fitted time series models. *Measurement Science and Technology*, 31(5):055008, 2020. doi:10.1088/1361-6501/ab5131.

19 Richard Leach. *Optical Measurement of Surface Topography*. Springer Berlin Heidelberg, Berlin, Heidelberg, 2011. doi:10.1007/978-3-642-12012-1.

20 Siavash Malektaji, Ivan T. Lima, and Sherif S. Sherif. Monte carlo simulation of optical coherence tomography for turbid media with arbitrary spatial distributions. *Journal of biomedical optics*, 19(4):046001, 2014. doi:10.1117/1.JBO.19.4.046001.

21 Adrian Gh. Podoleanu. Optical coherence tomography. *Journal of microscopy*, 247(3):209–219, 2012. doi:10.1111/j.1365-2818.2012.03619.x.

22 Tuukka Prykäri, Jakub Czajkowski, Erkki Alarousu, and Risto Myllylä. Optical coherence tomography as an accurate inspection and quality evaluation technique in paper industry. *Optical Review*, 17(3):218–222, 2010. doi:10.1007/s10043-010-0039-y.

23 Fernando Puente León and Jürgen Beyerer. Oberflächencharakterisierung durch morphologische filterung (surface characterization by morphological filtering). *tm - Technisches Messen*, 72(12/2005):602, 2005. doi:10.1524/teme.2005.72.12.663.

24 Maik Rahlves and Jörg Seewig. *Optisches Messen technischer Oberflächen: Messprinzipien und Begriffe*. Beuth Pocket. Beuth Verlag GmbH, 1. edition, 2009.

25 Yogesh Rao, N. P. Sarwade, and Roshan Makkar. Modeling and simulation of optical coherence tomography on virtual oct. *Procedia Computer Science*, 45:644–650, 2015. doi:10.1016/j.procs.2015.03.121.

26 Stefan Roth and Achim Stahl. *Optik*. Springer Berlin Heidelberg, Berlin, Heidelberg, 2019. doi:10.1007/978-3-662-59337-0.

27 Joanna Schmit. White-light interference 3d microscopes. In Kevin Harding, editor, *Handbook of Optical Dimensional Metrology*, pages 395–418. CRC Press, 2016.

28 Robert Schmitt, Friedel Koerfer, and Stephan Bichmann. Modellierung optischer messprozesse (modelling of optical measurement methods). *tm - Technisches Messen*, 75(4):6152, 2008. doi:10.1524/teme.2008.0832.

29 Robert Schmitt, Friedel Koerfer, Oliver Sawodny, Jan Zimmermann, Rolf Krüger-Sehm, Min Xu, Thorsten Dziomba, Ludger Koenders, Gert Goch, Andreas Tausendfreund, Stefan Patzelt, Sven Simon, Lars Rockstroh, Carsten Bellon, Andreas Staude, Peter Woias, Frank Goldschmidtböing, and Martin Rabold. Virtuelle messgeräte: Definition und stand der entwicklung (virtual measuring instruments: Definition and development status). *tm - Technisches Messen*, 75(5/2008):357, 2008. doi:10.1524/teme.2008.0872.

30 Heinrich Schwenke. *Abschätzung von Meßunsicherheiten durch Simulation an Beispielen aus der Fertigungsmeßtechnik: Zugl.: Chemnitz, Techn. Univ., Diss*, volume 36 of *PTB-Bericht F, Fertigungsmeßtechnik*. Bremerhaven Wirtschaftsverl. NW Verl. für neue Wissenschaft, Bremerhaven, 1999.

31 Jörg Seewig, Thomas Böttner, and Daniel Broschart. Uncertainty of height information in coherence scanning interferometry. In Peter H. Lehmann, Wolfgang Osten, and Kay Gastinger, editors, *Optical Measurement Systems for Industrial Inspection VII*, SPIE Proceedings, page 80820V. SPIE, 2011. doi:10.1117/12.889796.

32 Jörg Seewig, Matthias Eifler, Frank Schneider, Benjamin Kirsch, and Jan C. Aurich. A model-based approach for the calibration and traceability of the angle resolved scattering light sensor. *Surface Topography: Metrology and Properties*, 4(2):024010, 2016. doi:10.1088/2051-672X/4/2/024010.

33 Muhammad Faizan Shirazi, Kibeom Park, Ruchire Eranga Wijesinghe, Hyosang Jeong, Sangyeob Han, Pilun Kim, Mansik Jeon, and Jeehyun Kim. Fast industrial inspection of optical thin film using optical coherence tomography. *Sensors (Basel, Switzerland)*, 16(10), 2016. doi:10.3390/s16101598.

34 Lars Thrane. *Optical coherence tomography: Modeling and applications*, volume 1217 (EN) of *Risø-R*. Risø National Laboratory and Available from: Risø National Laboratory, Information Service Department, Roskilde, 2001.

35 Lars Thrane, Thomas M. Jørgensen, Mikkel Jørgensen, and Frederik C. Krebs. Application of optical coherence tomography (oct) as a 3-dimensional imaging technique for roll-to-roll coated polymer solar cells. *Solar Energy Materials and Solar Cells*, 97:181–185, 2012. doi:10.1016/j.solmat.2011.10.004.

36 Gerd R. Tillack, Christina Nockemann, and Carsten Bellon. X-ray modeling for industrial applications. *NDT & E International*, 33(7):481–488, 2000. doi:10.1016/S0963-8695(00)00019-0.

37 François M. Torner. *Entwicklung virtueller, optischer Sensoren zur Charakterisierung geometrischer Oberflächen*. Dissertation, Universität Kaiserslautern, 2018.

38 François M. Torner, Jayanti Das, Gerhard Stelzer, Barbara Linke, and Jörg Seewig. Fundamental analysis of the usability of an angle-resolved scattered light sensor for monitoring vibratory finishing processes based on ray tracing simulations. *Applied Mechanics and Materials*, 869:115–127, 2017. doi:10.4028/www.scientific.net/AMM.869.115.

39 François M. Torner, Gerhard Stelzer, Lukas Anslinger, and Jörg Seewig. Description and evaluation of a simplified model to simulate the optical behavior of an angle-resolved scattered light sensor. *Journal of Computing and Information Science in Engineering*, 17(2):31, 2017. doi:10.1115/1.4034386.

40 Andreas Tycho, Thomas M. Jørgensen, Harold T. Yura, and Peter E. Andersen. Derivation of a monte carlo method for modeling heterodyne detection in optical coherence tomography systems. *Applied optics*, 41(31):6676–6691, 2002. doi:10.1364/AO.41.006676.

41 Junxin Wang, Changgang Xu, Annica M. Nilsson, Daniel L. A. Fernandes, and Gunnar A. Niklasson. A novel phase function describing light scattering of layers containing colloidal nanospheres. *Nanoscale*, 11(15):7404–7413, 2019. doi:10.1039/C9NR01707K.

42 Lihong Wang, Steven L. Jacques, and Liqiong Zheng. Mcml—monte carlo modeling of light transport in multi-layered tissues. *Computer Methods and Programs in Biomedicine*, 47(2):131–146, 1995. doi:10.1016/0169-2607(95)01640-F.

43 Ashley J. Welch and Martin J.C. van Gemert. *Optical-Thermal Response of Laser-Irradiated Tissue*. Springer Netherlands, Dordrecht, 2011. doi:10.1007/978-90-481-8831-4.

44 Faming Xu, Haridas E. Pudavar, Prasad N. Prasad, and David L. Dickensheets. Confocal enhanced optical coherence tomography for nondestructive evaluation of paints and coatings. *Optics letters*, 24(24):1808–1810, 1999. doi:10.1364/OL.24.001808.

45 Min Xu, Thorsten Dziomba, and Ludger Koenders. Modelling and simulating scanning force microscopes for estimating measurement uncertainty: A virtual scanning force microscope. *Measurement Science and Technology*, 22(9):094004, 2011. doi:10.1088/0957-0233/22/9/094004.